



On the relationship between N content, textural properties and catalytic performance for the oxygen reduction reaction of N/CNT

Carlota Domínguez^a, Francisco J. Pérez-Alonso^{a,*}, Mohamed Abdel Salam^b, Shaeel A. Al-Thabaiti^b, Abdullah Y. Obaid^b, Abdulmohsen A. Alshehri^b, José L. Gómez de la Fuente^a, José L.G. Fierro^a, Sergio Rojas^{a,*}

^a Grupo de Energía y Química Sostenibles (EQS), Instituto de Catálisis y Petroleoquímica, CSIC, C/Marie Curie, 2, L10, 28049 Madrid, Spain

^b Chemistry Department, Faculty of Science, King Abdulaziz University, PO Box 80200, Jeddah 21589, Saudi Arabia

ARTICLE INFO

Article history:

Received 16 April 2014

Received in revised form 27 June 2014

Accepted 1 July 2014

Available online 9 July 2014

Keywords:

ORR

CNTs

Defects

NPMCs

Fuel cells

ABSTRACT

Non-precious metal catalysts for the oxygen reduction reaction (ORR) based upon the incorporation of different amounts of N into the C–C network of multiwalled carbon nanotubes (CNTs) have been prepared by using CNTs and urea as the carbon and nitrogen sources, respectively. First, and with the aim of generating different levels of defects in the carbon network, the CNTs have been subjected to ballmilling during different periods of time between 0 and 150 h. Then, urea was mixed with the treated CNTs, subjected to further ballmilling and pyrolyzed at 800 °C. The number of defects, and as a consequence, the amount of N incorporated into the CNTs, increases with the duration of the ballmilling time. Moreover, the structure of the CNTs obtained after longer ballmilling times collapses leading to a carbon material with a high degree of microporosity. The performance of the N/CNT for the ORR, in terms of both the onset potential and mass current activity, increases with the amount of N actually incorporated into the CNT. Moreover, the H₂O₂ formation during ORR varies with the morphology of the catalyst. Thus, the formation of H₂O₂ is favored with the electrocatalysts in which the CNT structure is preserved, whereas the total reduction of O₂ to H₂O is favored for the electrocatalysts in which micropores are formed.

© 2014 Elsevier B.V. All rights reserved.

1. Introduction

The increasing demand of primary energy, which is mainly coped by increasing the use of fossil fuels, has serious environmental and socioeconomical implications. As a consequence, most countries have embraced strong energy and environmental policies aimed to decreasing their dependence on fossil fuels and to control the level of harmful emissions. In this context, the use of C-decoupled sources of energies has emerged as an alternative to fossil fuels. Among those, H₂ has been recognized as an ideal energy vector since its production and transformation into useful energy can be achieved by fully C-decoupled technologies.

It is widely recognized that H₂-feed proton exchange membrane fuel cells (PEMFCs) are the ideal devices to transform chemical energy into electricity. As a consequence, they have been identified as ideal devices for powering transportation vehicles and

portable devices. In the current state-of-the-art, both the anode and cathode electrodes of PEMFCs are based upon carbon supported Pt nanosized particles. It is well admitted that Pt is the best catalyst for both hydrogen oxidation and oxygen reduction (ORR) reactions in acid media. However, due to the sluggish kinetics of the ORR, the amount of Pt used on the cathode electrode is too high, of *ca.* 0.5 mg_{Pt} cm⁻² [1] and as a consequence the price of PEMFCs is not yet competitive. Numerous attempts are addressed to decrease Pt loading on the cathode electrode and Department of Energy of US Government (DOE) has established a target loading of 0.15 mg_{Pt} cm⁻² for 2015 [2]. The most successful ones aim to enhance the exposed area by decreasing Pt size and to optimize Pt electronic properties towards oxygen adsorption and reduction by alloying Pt with metals such as Ni and Co. A disruptive approach consists in replacing Pt (or other noble metals for this matter) content altogether by using non-precious metal catalysts (NPMCs) which are less expensive and more abundant than noble metals [3]. As a rule of thumb, NPMCs exhibit lower intrinsic kinetics of for the ORR; however, this feature can be compensated by using higher amounts of NPMC without severe economic repercussions.

* Corresponding authors. Tel.: +34 91 585 4632.

E-mail addresses: fperez@icp.csic.es (F.J. Pérez-Alonso), srojas@icp.csic.es (S. Rojas).

In general, the more active NPMCs are based upon a transition metal inserted within a matrix of N-substituted graphitic carbon, usually referred to as M/N/C [3]. These catalysts are in fact based upon the pioneering work of Jasinski et al. who reported that cobalt phthalocyanine catalyzed the ORR in alkaline medium [4]. Although it is well documented that this type of NPMCs exhibit significant lower activities than Pt/C for the ORR in acid media, current densities as high as 230 A cm^{-2} at 0.8 V have been reported [5]. In general, the preparation of NPMCs comprises the intimate mixture by wet impregnation and/or mechanical process using planetary ball milling of a carbon matrix such as active carbon, carbon nanotubes or graphene or a carbon precursor, a transition metal (M) precursor and a nitrogen source followed by one or several thermal treatments. In order to obtain the active sites for the ORR, thermal treatments must be conducted at of 600°C or higher either under inert or reactive (NH_3) atmospheres. Previous works have concluded that N atoms from a N-rich polymer precursor are anchored within the carbon matrix leading to the formation of the active sites during the thermal treatment [6,7]. In addition, during this thermal process micropores are generated and as a result higher ORR activities are recorded [8].

The actual arrangement of the N, M and C atoms at the active sites for the ORR is elusive. The first hypothesis proposed three decades ago claimed that N and C atoms are the real active sites of the NPMCs for the ORR [9,10]. More recent studies sustain, however, that the active sites consist of a non-precious metal such as Fe, Co or Mn coordinated to an undetermined number of N atoms inserted onto a carbon matrix [3,11,12]. In this line, a recent study recognized the ORR ability of M/N/C M=Fe, Co and Mn follows the order $\text{Fe} > \text{Co} > \text{Mn}$ [13]. It is worth to remark that although most works coincide in that the transition metal should be present during the thermal treatment step in order to generate active catalysts for the ORR it is still under debate whether the transition metal is an indispensable element of the active site itself or whether it only serves to create the active sites but it is unclear whether it does actually participate in the turnover cycles [14–16].

Several types of carbons and carbon sources have been employed for the synthesis of NPMCs. In general, the most active catalysts for the ORR are obtained when the final catalyst has a large fraction of micropores or when they are created during thermal treatments. On the other hand, a recent study about the durability of NPMCs reports that CNTs render more durable catalysts than carbon blacks [17].

As stated above, N atoms are necessary to create the active site for the ORR. The following N species have been detected upon N incorporation into graphitic structures; pyridinic, pyrrolic, graphitic (or quaternary) and oxidized N. The ratio of these species varies with the N precursor and thermal treatment. The role of the different N species controversial and studies pointing to each one of these N species as the main responsible for the ORR activity exist. Recently, Yasuda et al. have reported that pyridinic N promotes the ORR via a four-electron pathway whereas graphitic N promotes the indirect reduction of O_2 via a two-electron pathway, i.e., through the formation of H_2O_2 [18], revealing that different nitrogen species are anchored to the carbon matrix differently, in the case of graphene and carbon nanotubes, pyridinic-N is placed at the edge of the graphene planes and CNTs whereas quaternary-N could substitute carbon atoms within graphitic network and the graphene layer and it is also placed at the edge of the carbon source [18,19].

Recently, FeN_4 and FeN_{2+2} ensembles have been identified as the real active sites for the ORR with Fe-based NPMCs [20–23]. Some studies went further and highlighted the importance of the protonation of the N atoms coordinated to the metal atom and/or of N atoms adjacent to the Fe/N sites for the ORR [7,22,23].

Regardless of the actual role of N for the ORR, it appears like the catalytic performance of NPMCs increases with the amount of N onto the catalyst which is in turn related with the amount of defects into carbon nanotubes [24]. The aim of this work is to understand the relationship between the amount of defects of a carbon matrix (CNTs) and the incorporation of N into the carbon network and the repercussions for the ORR in acid medium. In a first step we aimed to generate controllable amounts of defects into CNTs by subjecting CNTs to increasing ballmilling periods. Then, N was incorporated onto the treated CNTs by a further ballmilling step followed by a thermal treatment in N_2 . Finally, the performance of the catalysts obtained for the ORR in acid medium was evaluated by electrochemical techniques.

2. Experimental

2.1. Synthesis of NPMCs

A series of NPMC have been synthesized by means of a mechanical method consisting in two sequential ballmilling steps under r.t. conditions, employing a planetary ball mill (PM100, Retsch), followed by a thermal treatment under inert atmosphere. Multi-walled carbon nanotubes were used as the carbon matrix (CNTs, SUNANO; purity > 90%, Syn Nanotech Co Ltd) and urea ($\text{CH}_4\text{N}_2\text{O}$, PANREAC PRS) was used as the N-precursor. Previous to further treatments, CNTs were subjected to an acid leaching with HNO_3 20% v/v at 110°C for 5 h to eliminate contaminants [25]. The vessel employed during ballmilling treatment is made of stainless steel; 10 mm diameter stainless steel balls were used. First, the CNTs were ballmilled for different periods of time of 0, 12, 24, 48, 72 or 150 h, with the aim to generate an increasing number of defects and/or edges in the ballmilled CNTs, thereby increasing materials' ability to incorporate heteroatoms such as N or Fe, thus leading to a greater density of active sites. The materials obtained were referred to as CNT-t, where t denotes the time under ballmilling. Then, urea and CNT-t (molar ratio CNT-t:Urea 2:1) were intimately mixed by ballmilling for 24 h. The samples recovered were subjected to a thermal treatment in a quartz tubular reactor at 800°C (heating ramp of $20^\circ\text{C min}^{-1}$ under an inert atmosphere of 25 mL min^{-1} N_2 for 1 h). At this temperature, all samples loose ca. 70 wt% of their initial mass as shown in Fig. S1 (Supplementary material). The incorporation of the N atoms within the C sp^2 matrix was achieved during this thermal step [6]. The samples recovered after the thermal treatment were labeled as N/CNT-t.

2.2. Physicochemical characterization

Carbon, nitrogen and hydrogen weight contents were measured with an elemental analyser (LECO CHNS-932).

X-ray photoelectron spectra (XPS) were acquired with a VG Escalab 200R spectrometer fitted with an $\text{Mg K}\alpha$ ($h\nu = 1253.6\text{ eV}$) 120 W X-ray source. The energy regions of the photoelectrons of interest were scanned until an acceptable signal-to-noise ratio was achieved. Intensities were estimated by calculating the integral of each peak after subtraction of the Shirley-type background and fitting of the experimental curve to a combination of Lorentzian and Gaussian lines of variable proportions. Accurate binding energies ($\pm 0.2\text{ eV}$) were determined by setting the most intense C 1s peak at 284.6 eV .

Raman spectra were recorded in air using a single monochromator Renishaw system 1000 equipped with a thermoelectrically cooled CCD detector and holographic super-Notch filter. The samples were excited with the 532 nm Ar line. The instrument is internally calibrated with a silicon reference at 520 cm^{-1} and gives a peak position resolution of 1 cm^{-1} , the spectrum acquisition time

was 10 s and 5 spectra were acquired to ensure an optimal signal to noise ratio.

X-ray diffractograms were collected on a Seifert 3000 powder diffractometer operating with Cu K α radiation ($\lambda = 0.15418$ nm) generated at 40 kV and 40 mA. Scans were recorded at 0.02° s $^{-1}$ for 2θ values between 10° and 90° .

Textural properties were evaluated by N₂ adsorption-desorption isotherms of the samples recorded at liquid N₂ temperature with a Micromeritics ASAP 2000 apparatus. Samples were degassed at 140° C under vacuum for 24 h. Specific areas were calculated by applying the BET method within the relative pressure range $P/P^0 = 0.05–0.30$.

The transmissions electron microscopy (TEM) images of the samples were collected using a JEOL JEM 2100FX microscope operating at 200 keV, point resolution of 0.31 nm. The specimens for analysis were prepared by dispersing the powdered samples in a mixture of isopropanol and Milli-Q water using an ultrasonic bath. A drop of each resulting suspension was placed on a copper grid covered with a porous carbon film.

The Fe wt.% composition of the solids was determined by inductively coupled plasma emission spectrometry (ICP-OES) using a Perkin-Elmer Optima 3300DV apparatus.

2.3. Electrochemical characterization

The electrochemical experiments were performed with a computer controlled Autolab PGstat 302N potentiostat/galvanostat. A standard three-compartment glass cell and a rotating disk electrode (RDE) (Pine research Instruments) were used for all electrochemical experiments. The counter electrode was a graphite rod and the reference electrode was a homemade RHE electrode.

A glassy carbon electrode with a thin film of the electrocatalyst under study was used as the working electrode. For the thin film preparation, samples were dispersed ultrasonically for 10 min in a mixture of Millipore Milli Q® water, isopropyl alcohol (Aldrich, 99.8%) and Nafion (5 wt%) with a final ratio of 80, 18.8 and 0.2 vol%, respectively. The final concentration of the electrocatalyst in the suspension was of $6 \text{ mg}_{\text{cat}} \text{ mL}^{-1}$. A volume of $20 \mu\text{L}$ of the suspension was pipetted onto the previously polished glassy carbon tip of the RDE.

Previous to the electrochemical testing, the working electrode was electrochemically cleaned by potential cycling from 0.05 to 1.1 V vs. RHE for 50 cycles in Ar-saturated 0.1 M HClO₄ electrolyte. Cyclic voltammograms (CVs) were recorded between 0.05 and 1.03 V at 10 mV s^{-1} in Ar-saturated 0.1 M HClO₄.

The ORR polarization curves were collected by means of the RDE technique between 0.05 V and 1.03 V at 10 mV s^{-1} and 1600 rpm in O₂-saturated 0.1 M HClO₄ electrolyte. The Faradaic current density (j_{F} mA cm $^{-2}$) was obtained by subtracting the current obtained during the anodic sweep scan in the O₂-saturated electrolyte from the capacitive current (density) obtained in the potential sweep recorded in Ar-saturated O₂-free electrolyte under the same experimental conditions. The ORR kinetic current (i_{K}) was calculated from the Koutecky-Levich equation ($i_{\text{K}} = -j_{\text{F}} \times i_{\text{lim}} / (i_{\text{F}} - i_{\text{lim}})$) where i_{K} is

the kinetic current and i_{lim} is the limiting current. Finally, the ORR mass activity is defined by $i_{\text{M}} = -i_{\text{K}} / m_{\text{cat}}$ where m_{cat} is the catalyst loading expressed in g [11]. H₂O₂ production were recorded using a rotating ring disk electrode (RRDE) which ring is made of platinum, under the same experimental conditions than that reported above for the RDE experiments, *i.e.*, recording a linear sweep voltammetry scan between 0.05 V and 1.03 V at 10 mV s^{-1} and 1600 rpm in O₂-saturated 0.1 M HClO₄ electrolyte while applying a constant ring potential of 1.2 V. The fraction of H₂O₂ produced was calculated according to the next equation:

$$(1) X_{\text{H}_2\text{O}_2} = \frac{2I_{\text{R}}/N}{I_{\text{D}}+I_{\text{R}}/N} \text{ where } I_{\text{D}} \text{ is the disk current and } I_{\text{R}} \text{ is the ring current and using a ring efficiency (N) of 26\% [26].}$$

In order to determine whether Fe impurities are responsible for the ORR activity selected catalysts were poisoned with thiocyanate in order to suppress the activity of the Fe sites. For this matter, selected catalysts were deposited onto the working electrode (see above) and immersed in a 0.01 M solution of NaSCN (Aldrich >99.99%) during 15 min at 1000 rpm. Then, ORR polarization curves were recorded following a protocol identical as that described above.

3. Results and discussion

3.1. Physicochemical characterization of CNT-t and N/CNT-t

The bulk C, H and N contents obtained from elemental analysis are shown in Table 1. The results obtained clearly show that the amount N incorporated into the samples increases with the duration of the ballmilling treatment from 0.66 in N/CNT-0 to 3.94 wt% in N/CNT-150. This results are in line with previous works using other carbon supports (black pearls and carbon black), in which a similar trend was observed [27,28]. However, a careful inspection of the evolution of the N contents with the ballmilling time reveals that the incorporation of N is only moderate for the CNT-t subjected to ballmilling periods between 0 and 48 h but increases dramatically for the CNT-t ballmilled for longer periods of time of 72 and 150 h.

Table 1 also shows that the combined amount of C, H and N is lower than 100% and that it decreases with the increasing ballmilling time indicating that other elements might be incorporated into the samples after ballmilling. In addition to the presence of oxygen and metals used for the synthesis of the CNTs (see Section 3 for N/CNT-0), previous studies have shown that Fe species become incorporated even encapsulated within the carbon matrix during the ballmilling process. This effect will be addressed below. The C 1s, N 1s and O 1s core-level spectra of the different samples were recorded in order to estimate the relative surface abundance of the elements and to identify the nature of the N species and their evolution during ballmilling. The N 1s spectra, show in Fig. 1 have been fitted to four components with peak maxima at 398.5, 400.1, 401–401.5 and 403.4–404 eV, respectively. The FWHM for all N 1s peaks is of around 2. In view of these binding energy values, the N species have been ascribed to pyridinic-N, pyrrolic-N, graphitic-N and N-oxide species, respectively [3,11].

Table 1

C, N and H content determined by elemental analysis and N/C weight ratios.

Sample	Weight content (%)			N/C weight ratio	N/C atomic ratio
	C	H	N		
N/CNT-0	93.91	0.14	0.66	0.007	0.006
N/CNT-12	92.21	0.21	0.84	0.009	0.008
N/CNT-24	90.76	0.26	1.23	0.014	0.012
N/CNT-48	91.11	0.30	1.20	0.013	0.011
N/CNT-72	89.12	0.58	1.75	0.020	0.017
N/CNT-150	84.58	0.97	3.94	0.047	0.040

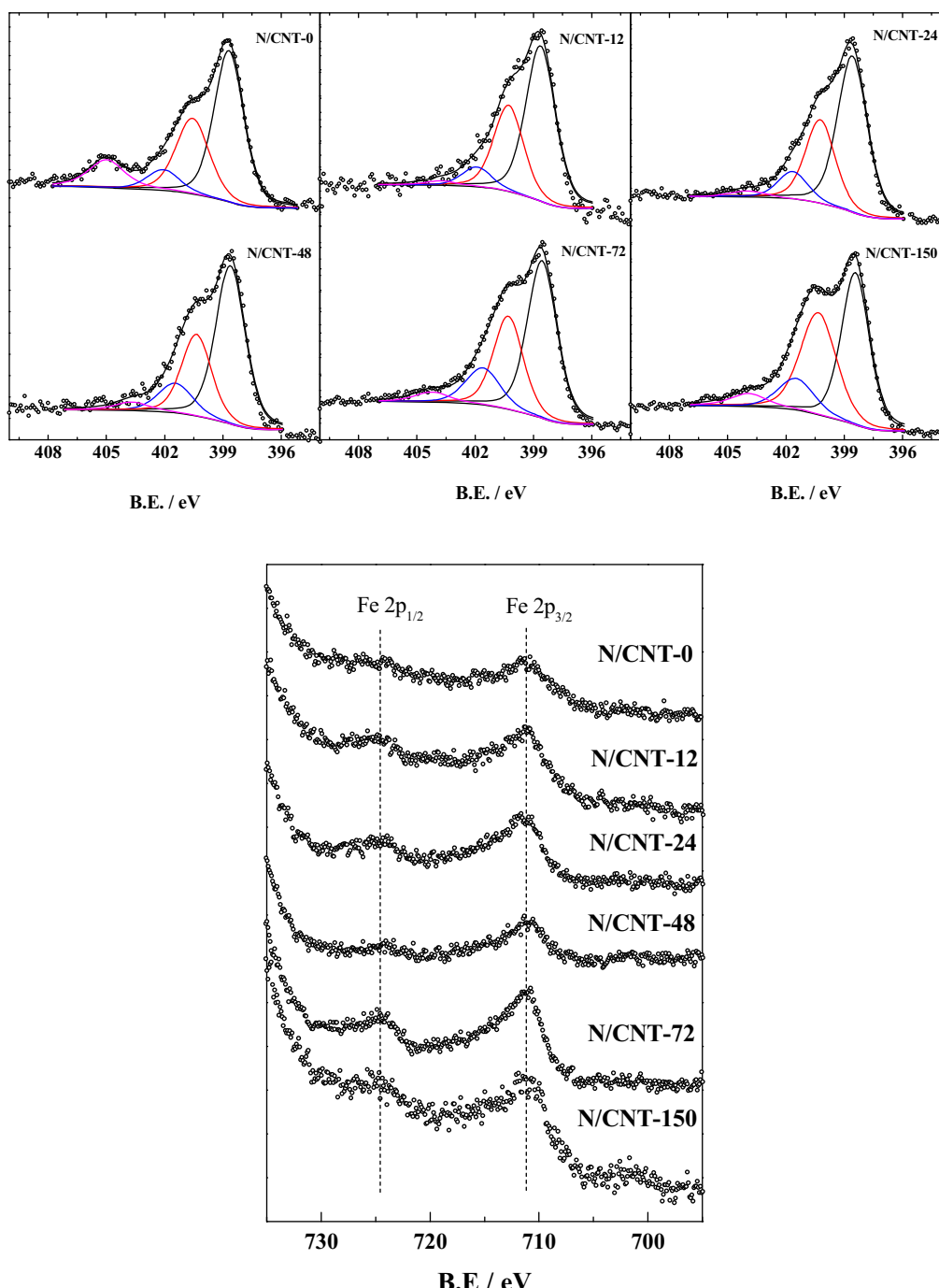


Fig. 1. (a) N 1s core-level spectra of the N/CNT-t samples (black line). Peaks for N-pyridinic, N-pyrrolic, N-quaternary and oxidized N are shown in black, red, blue and magenta. (b) Fe 2p core-level spectra of N/CNT-t samples. (For interpretation of the references to color in this figure legend, the reader is referred to the web version of this article.)

Table 2
Surface abundance of N, Fe and O and distribution of N species.

Sample	Surface atomic ratios			ratio of surface N species			
	N/C	Fe/C	O/C	N _{pyridinic}	N _{pyrrolic}	N _{graphitic}	N _{oxide}
CNT _{pristine}	0.003	n.d.	0.052	0.43	0	0.16	0.41
N/CNT-0	0.019	0.0007	0.045	0.51	0.28	0.08	0.13
N/CNT-12	0.010	0.0010	0.042	0.58	0.32	0.07	0.02
N/CNT-24	0.017	0.0010	0.047	0.57	0.30	0.10	0.02
N/CNT-48	0.012	0.0005	0.052	0.55	0.29	0.12	0.04
N/CNT-72	0.019	0.0012	0.062	0.51	0.30	0.14	0.04
N/CNT-150	0.038	0.0018	0.064	0.49	0.34	0.12	0.05

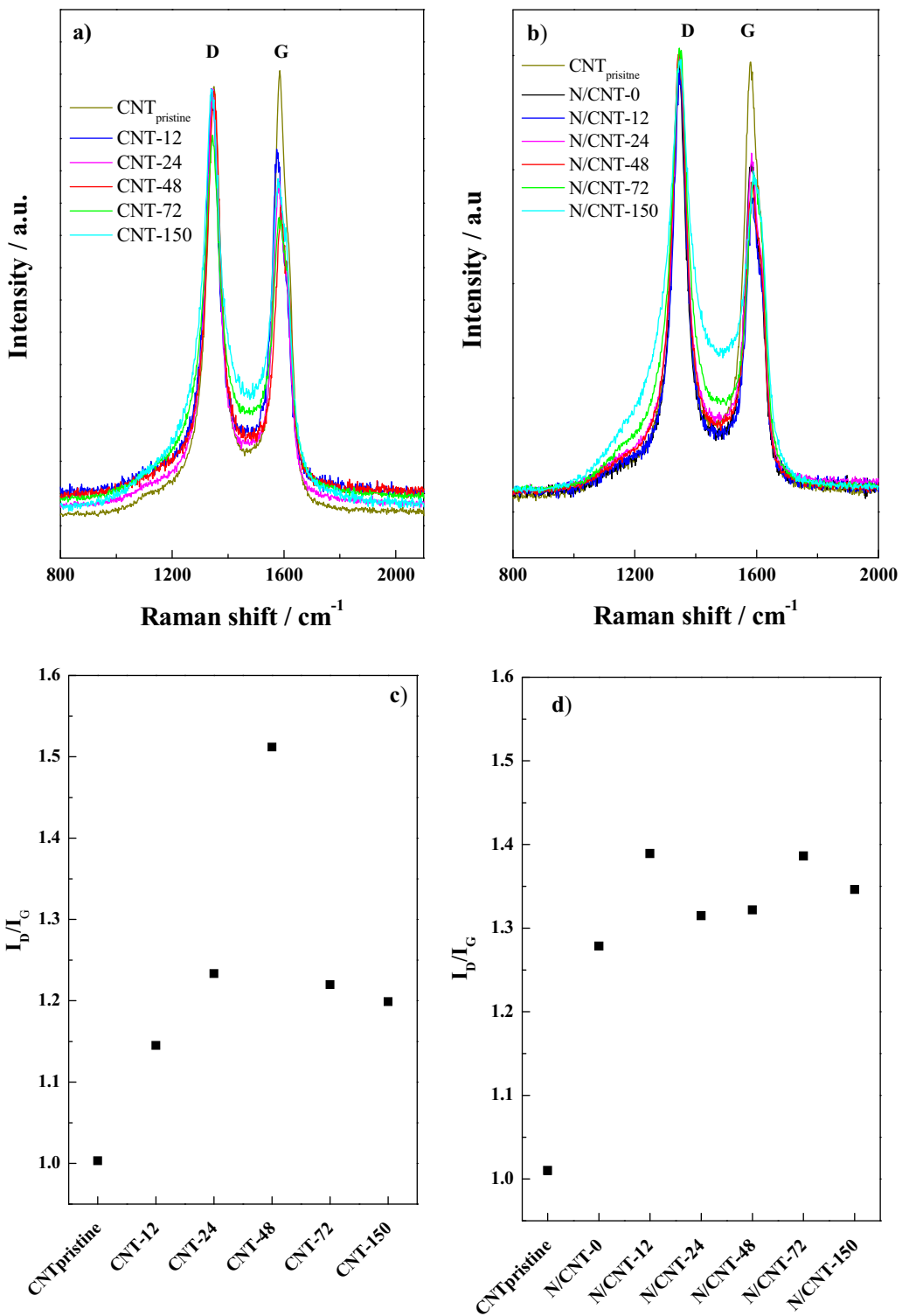


Fig. 2. Evolution of the Raman spectra recorded for (a) the CNTs subjected to different ballmilling times (CNT-t), (b) the final catalysts N/CNT-t. The spectrum of the fresh CNT is included for comparison. Evolution of the I_D/I_G ratio for (c) CNT-t and (d) N/CNT-t.

A careful comparison between the bulk and surface N/C atomic ratios reported, respectively, in Tables 1 and 2 indicate that the N atoms incorporated on the CNTs subjected to a previous ballmilling process, *i.e.*, all CNTs except CNT-0, are preferentially distributed on the surface of the catalyst. It is remarkable a higher surface enrichment of N for sample N/CNT-0 and N/CNT-24.

Four different surface N-species are detected by XPS in all samples, including the fresh CNT (spectrum not shown). Remarkably,

the amount of oxidized N (characterized by the peak at the highest binding energy) is of *ca.* 41 at% in the fresh CNT (see Table 2) decreasing significantly for the samples subjected to ballmilling. In the same line, previous works suggest that pyridinic-N has an important role in the ORR activity [18,29] by favouring the so-called four-electron pathway (direct reduction of O_2 to H_2O) as compared to N-graphitic which seems to promote the so called two-electron pathway. According to the results shown in Table 2,

the amount of N-pyridinic in the N/CNT-t ranges between *ca.* 50 at% and 60 at% whereas the amount of N-graphitic is much lower, ranging between 7 at% and 14 at%. The proportion of N-graphitic and N-pyridinic species are not severely affected by the duration of the ballmilling treatment.

The presence of Fe in the N/CNT-t and its evolution with ballmilling time has been monitored by XPS. Fig. 1b shows the Fe 2p core-level region of all samples. The binding energy of the Fe 2p_{3/2} peak is centered at *ca.* 711 eV. This binding energy is usually assigned to the presence of Fe³⁺ species although in some cases it has also been assigned to Fe²⁺ or to FeOOH species. The presence of Fe³⁺ usually leads to the observation of a shake-up satellite peak at *ca.* 719.2 eV, which is the fingerprint of the Fe³⁺ species [30]. However, this satellite peak is only observed in the spectrum for N-CNT-12, although due to the low intensity of the signals the presence of Fe³⁺ species is not excluded in the other spectra. As shown in Table 2, the amount of Fe (reported as Fe/C atomic ratio) is similar in all samples and in fact it follows no clear trend with the duration of the ballmilling treatment. Although not shown, the amount of Fe in the pristine CNT (before subjected to ballmilling) is of *ca.* 0.7 wt% as deduced from ICP-OES analysis. Since Fe is not detected by XPS in the fresh CNT it is reasonable to assume that the iron species remain encapsulated within several carbon layers. These results indicate that the incorporation of Fe into the final CNTs is not due only to the ballmilling process from wear steel vessel used during synthesis. The actual amount of Fe in N-CNT-48 was also analyzed by ICP-OES, obtaining a value of 1.27 wt%. The evolution of the structural defects in the CNTs with the ballmilling time was studied by Raman spectroscopy. In general, the Raman spectra of graphitic materials exhibit three characteristic bands at 1580 cm⁻¹, 1351 cm⁻¹ and 2700 cm⁻¹ which are usually referred to as G, D and 2D bands, respectively [19,31]. The G band is caused by the stretching of the C–C bond in graphitic materials appearing in all sp² carbon systems. [32]. On the other hand, both D and 2D bands are related to the degree of disorder of the carbon structure [33]. Therefore, the consequences of the ballmilling time for the creation of defects on the carbon structure of the CNTs can be assessed by recording the evolution of the normalized intensities of the D and G bands (*I*_D/*I*_G) bands. Fig. 2a depicts the first order Raman spectra of the CNT-t showing, for all samples, the expected D and G bands. The Raman spectra depicted in Fig. 2a and b shows a decreasing of the G band with the increasing ballmilling time, which is indicative of the loss of crystallinity of the CNTs during the treatment and to the creation of a greater number of defects. In addition, it can be observed how the D band slight broadens with the increasing ballmilling time. This effect could be indicative of the incorporation of N which would increase the structural imperfection of CNTs, specially pyridinic-N and graphitic-N [19]. The evolution of the *I*_D/*I*_G bands is shown in Fig. 2c and d; as observed, the ratio of the *I*_D/*I*_G bands increases after 12 h of ballmilling and then it remains roughly constant irrespective of the duration of the treatment.

The evolution of the crystallite size of the N/CNT-t has been followed by XRD analysis (Fig. 3). Crystallite size has been measured by applying the Scherrer equation to the most intense 002 peak at *ca.* 25°. The calculated particle size is of 3.7 ± 0.2 nm for the samples subjected to ballmilling periods *t* ≤ 48 h. This value is similar to that calculated for the pristine CNT of 3.8 nm. On the other hand, the catalysts prepared using the CNTs subjected to longer ballmilling periods exhibit smaller crystallites sizes of 2.9 and 1.9 nm for N/CNT-72 and N/CNT-150. These results suggest that a drastic change in the nature of the samples takes place after 72 h of ballmilling.

Table 3 shows the BET surface area, external surface and micropore surface values of all samples studied. The BET values recorded for the CNT-t remain roughly invariable, or exhibit a slight decrease, for the CNTs subjected to ballmilling periods of up to 48 h; *i.e.*

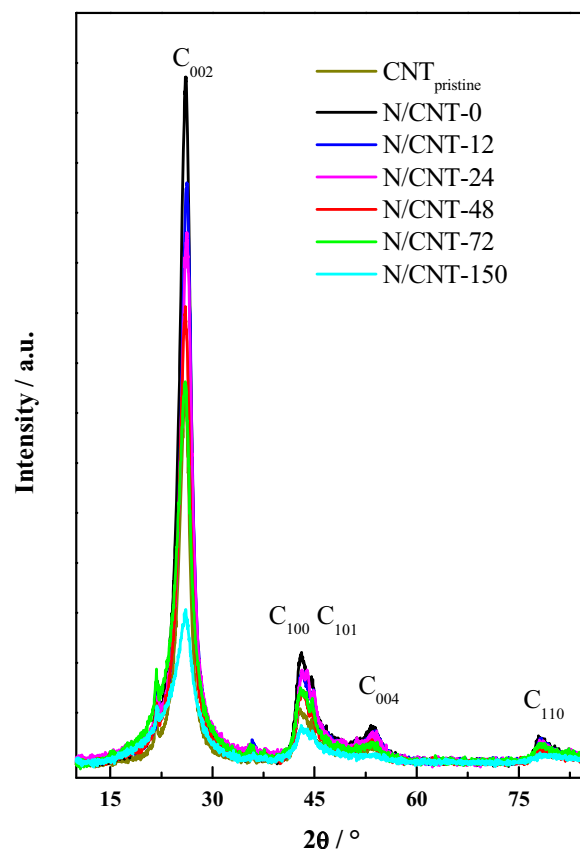


Fig. 3. X-ray diffractograms of the N/CNT-t. The diffractogram of the pristine CNT is shown for comparison. All diffraction peaks are ascribed to hexagonal graphite (pdf no. 01-075-1621).

CNT-12, CNT-24 and CNT-48. However, the BET values of the CNTs subjected to longer ballmilling periods increase significantly from 212 m² g⁻¹ recorded for the fresh CNT, to 486 and 524 m² g⁻¹ recorded for CNT-72 and CNT-150, respectively. This significant increasing of the BET area is due to the generation of microporosity during ballmilling. Thus, CNT-72 and CNT-150 record micropore surface areas of 150 and 169 m² g⁻¹, respectively, as compared to 13 m² g⁻¹ recorded for the fresh CNT. This is an important feature since it has been reported previously that the real active sites for the ORR in NPMCs are hosted within the micropores of the carbon matrix [6–8].

Table 3

BET area, external surface and micropore surface corresponding to carbon nanotubes samples after ball milling times (CNT-t) and samples after to being mixed with nitrogen precursor and heat treatment (N/CNT-t).

Sample	BET surface area (m ² g ⁻¹)	External surface area (m ² g ⁻¹)	Micropore surface area (m ² g ⁻¹)
CNT _{pristine}	212	199	13
CNT-12	218	211	7
CNT-24	208	196	12
CNT-48	209	191	18
CNT-72	486	336	150
CNT-150	524	355	169
N/CNT-0	229	227	3
N/CNT-12	239	235	4
N/CNT-24	237	228	9
N/CNT-48	235	224	12
N/CNT-72	392	283	109
N/CNT-150	483	288	195

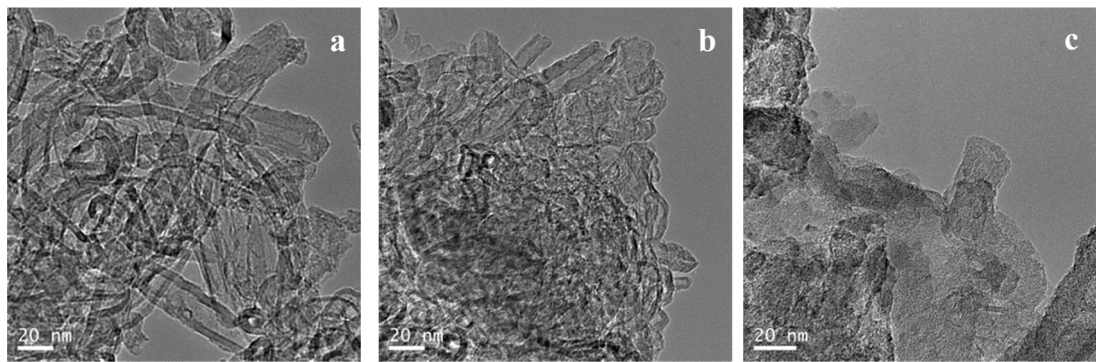


Fig. 4. Selected TEM images of (a) N/CNT-0, (b) N/CNT-48 and (c) N/CNT-150 recorded at the same magnification.

As also shown in **Table 3** the BET values recorded after N incorporation increases moderately for the samples without micropores in their structure, CNT-0, CNT-12, CNT-24 and CNT-48, decreasing for the catalysts prepared with CNT-72 and CNT-150. This decreasing account to the lower external and micropore surface area, so if NPCM active sites are effectively formed by MN_4 , they could be created in both sites (external and micropore surface). Note that N/CNT-150 catalyst increases the area correspond to micropores area after urea mixed and later pyrolysis steps. It is also important to note that external surface area is almost the same for N/CNT-72 and N/CNT-150 catalysts.

The effect of the duration of the ballmilling process for the morphology of the CNT-t has been assessed by recording TEM images of the samples, see **Fig. 4**.

CNTs are clearly observed in the TEM micrograph of N/CNT-0. Although CNTs are still observed in the image for N/CNT-48 a large fraction of amorphous carbon is also present in this sample. In addition, the CNTs are visible shorter in N/CNT-48. Finally, CNTs are almost absent the micrographs recorded with N/CNT-150 and instead amorphous carbon is the main structure observed in the micrographs.

3.2. Performance of N/CNT-t for the ORR

Fig. 5 shows the cyclic voltammograms (CVs) for all of the N/CNT-t electrocatalysts recorded at 10 mV s^{-1} in 0.1 M HClO_4 in

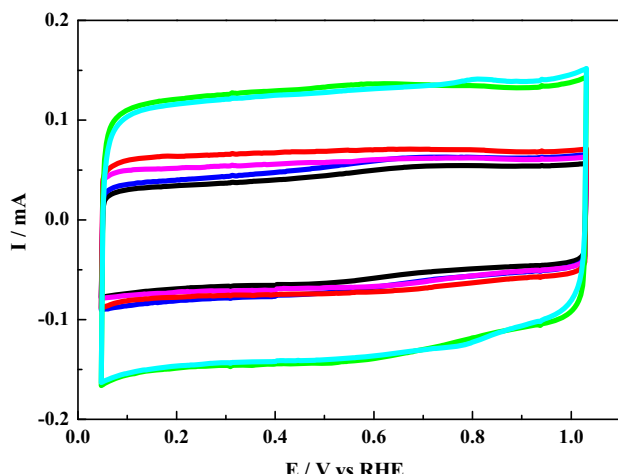


Fig. 5. Cyclic voltammograms for N/CNT-t recorded at 10 mV s^{-1} in 0.1 M HClO_4 . Catalyst loading 0.6 mg cm^{-2} . N/CNT-0 (black), N/CNT-12 (blue), N/CNT-24 (magenta), N/CNT-48 (red), N/CNT-72 (green) and N/CNT-150 (cyan). (For interpretation of the references to color in this figure legend, the reader is referred to the web version of this article.)

Ar saturated solution. The CVs show a squared wave profile, typical of potential independent capacitive responses [11]. As expected, the capacitive currents increase with the area of the catalysts and N/CNT-72 and N/CNT-150 record the greatest values in the series. In view of the results in **Table 3**, it appears like the intensity of the capacitive response may be related to external surface area because samples which external areas values are highly similar also present similar capacitive current values (N/CNT-72 and N/CNT-150).

Fig. 6a shows the ORR polarization curves of all N/CNT-t samples recorded during the positive going sweep in O_2 saturated 0.1 M HClO_4 electrolyte at 10 mV s^{-1} and 1600 rpm after subtraction of the corresponding capacitive currents. It should be noted that N/CNT-t are the only samples which record measurable activities for the ORR whereas CNT-t are inactive for the ORR. The ORR curves for all N/CNT-t exhibit a mixed kinetic controlled and a diffusion controlled region. A trend for the ORR can be clearly observed and the onset potential for the ORR shifts to more positive values as the amount of N in the catalyst increases. Thus, the onset potentials for N/CNT-0 and N/CNT-150 are of 0.72 and 0.84 V, respectively. These values are the less positive and the more positive in the series and clearly illustrate that the increasing amount of N in the final catalyst results in more active catalysts for the ORR. Not only the onset potential varies with the amount of N in the catalysts, but also higher current densities between 0.6 and 1.0 V are recorded as the amount of N in the catalyst increases, i.e., for the catalysts subjected to longer ballmilling treatments. **Fig. 6b** displays the normalized mass activities (i_M) (faradaic current values normalized to the mass of catalyst on the electrode) for all catalysts. As expected, the mass activity values increase with the increasing amount of N in the catalyst and N/CNT-150 records the highest mass activity in the series of 0.547 A g^{-1} at 0.8 V.

The results presented so far clearly illustrate that the duration of the ballmilling treatment has strong consequences in the morphology and textural properties of CNTs affecting both the incorporation of N and as a consequence the performance of the final catalysts for the ORR. However, not all of such effects are affected in the same way by ballmilling time. For instance, the morphology of the CNTs is severely affected after ballmilling treatments during 72 h or longer. Whereas CNTs are actually observed by TEM in the CNT-t subjected to ballmilling during $t \leq 48 \text{ h}$, the structure of the CNTs collapses after 72 h of ballmilling and nanotubes are not observed in the micrographs of CNT-72 and CNT-150. In line with this observation, the BET areas of the CNT-t remain roughly constant for ballmilling times of up to 48 h, increasing swiftly for the CNT-t subjected to 72 and 150 h of ballmilling. The increasing BET areas for these latter samples is due to the generation of a high degree of microporosity after ballmilling periods $\geq 72 \text{ h}$. As observed by TEM, the formation of micropores is due to the collapse of the structure of the CNTs. On the other hand, the generation of defects in the sp^2 structure of the CNTs, measured as the I_D/I_G ratio, reaches a plateau after 12 h of

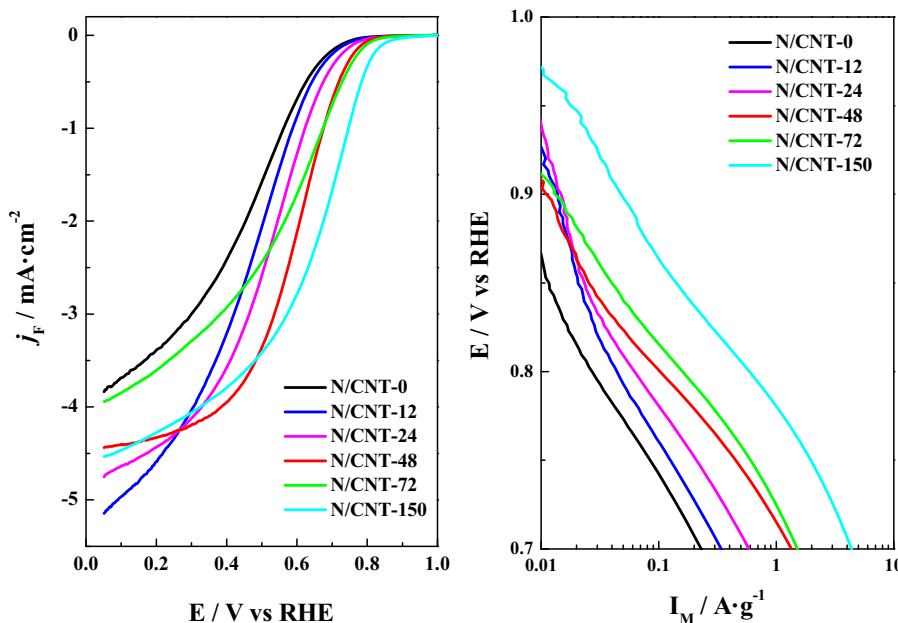


Fig. 6. (a) Faradaic current densities (j_F) and (b) mass activity (i_M) of all N/CNT-t recorded during the positive going sweep in oxygen saturated 0.1 M at 10 mVs^{-1} , 1600 rpm. Catalyst loading 0.6 mg cm^{-2} .

ballmilling. Finally, the incorporation of N increases with the higher ballmilling time of the CNT-t.

Before addressing the effects of the amount of N into the CNTs and of the development of porosity due to the collapse of the structure of the CNTs during ballmilling for the ORR we shall discuss the effect of the presence of residual iron for the ORR. It is well documented that cyanide adsorbs strongly on metals such as Fe or platinum group metals hence suppressing their activity for the ORR [34–36]. Since ORR experiments have been conducted at $\text{pH} \sim 1$, we used thiocyanate rather than cyanide to block the Fe sites. In order adsorb thiocyanate onto the selected catalysts: N/CNT-150, N/CNT-48 or N/CNT-0, the catalyst was deposited onto a rotatory electrode (see Section 2 for the disposition procedure) immersed in a 0.01 M solution of NaSCN in distilled H_2O during 15 min under rotation at 1000 rpm and rinsed Milli-Q water. Fig. 7 shows the performance of N/CNT-150, N/CNT-48 and N/CNT-0 for the ORR before and after thiocyanate adsorption. As observed, the ORR performance of all catalysts is moderately affected by the presence of thiocyanate, recording ca. 10–15% lower i_M values after thiocyanate adsorption. This observation indicates that the residual iron species detected by XPS are active for the ORR, but they are not the main responsible for the overall ORR performance of the catalysts. Moreover, Fig. 7 also shows that all catalysts show a similar level of deactivation upon thiocyanate adsorption so the trends in the ORR activity shown in Fig. 6, i.e., increasing i_M for the ORR with the increasing N-content.

As shown in Fig. 8, the mass activity (i_M) for the ORR at 0.8 V goes in parallel with the amount of N in the catalysts. A similar trend can be observed between the i_M and the micropore area, but no such trend between i_M and Fe content can be observed (see Fig. S2 in Supplementary material). The observed increasing of the i_M with the increasing amount of N demonstrates that in order to obtain more active catalysts for the ORR is necessary to designing synthetic strategies which allow incorporating higher amounts of N in the catalysts. However, two regimes for the incorporation of N into CNTs, and as a consequence for the ORR performance, can be observed. First, the incorporation of N increases only moderately for the CNT-t subjected to ballmilling periods ≤ 48 h. In fact, the amount of N actually incorporated into the CNTs increases linearly with the increasing amount of defects in the CNTs, which increases

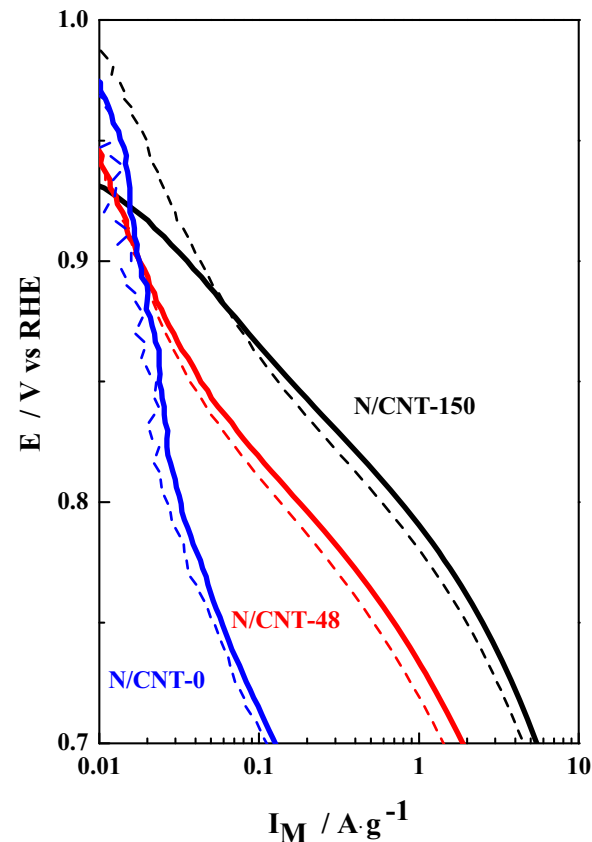


Fig. 7. Mass activity for the ORR recorded with N/CNT-150 (straight black line), N/CNT-48 (straight red line) and N/CNT-0 (straight blue line) in 0.1 M HClO_4 at 10 mVs^{-1} and 1600 rpm. Dotted lines are the mass activities recorded with the SCN-doped electrodes under the same reaction conditions. (For interpretation of the references to color in this figure legend, the reader is referred to the web version of this article.)

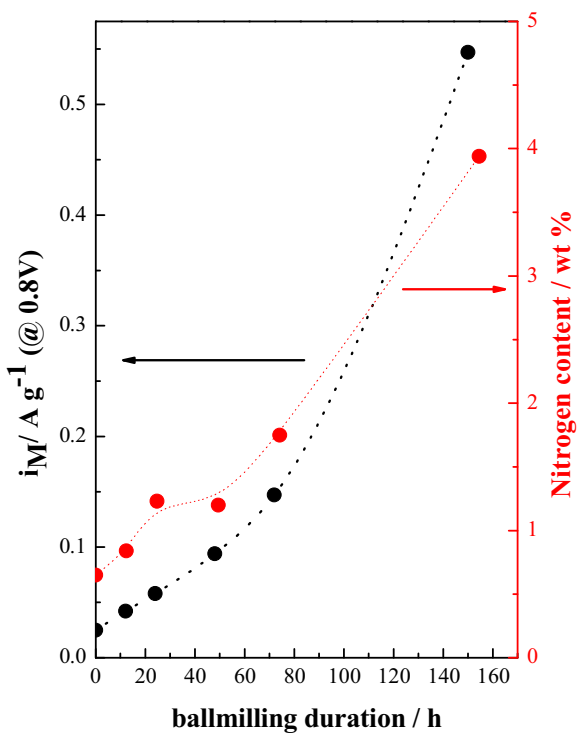


Fig. 8. Evolution of mass activity (i_M) recorded at 0.8 V (black line) and nitrogen content (wt%) (red line) with ballmilling time for N/CNT-t. (For interpretation of the references to color in this figure legend, the reader is referred to the web version of this article.)

moderately with the ballmilling time. On the other hand, the incorporation of N increases significantly for the CNT-t subjected to longer ballmilling periods of 72 and 150 h and so it does the ORR activity. Remarkably, Raman analyses indicate that the CNTs subjected to longer ballmilling periods contain a similar amount of defects than the ones subjected to treatments between 12 and 48 h suggesting that the present of defects is not the only feature controlling the incorporation of N into carbon based NPMCs. As stated above, the CNTs subjected to longer ballmilling periods exhibit significantly higher BET areas due to the generation of micropores. It is plausible to assume that this increasing of the BET area would result in a higher fraction of sites available for the incorporation of N. As shown in Fig. 8 the performance for the ORR increases with the amount of N in the catalysts. This trend applies to all samples regardless of their textural properties. However, Fig. 8 also shows that the formation of micropores, due to the collapse of the nanotubes' structure, leads to the formation of more active sites for the ORR. As shown in Fig. 8, mass activity of the active sites generated within the micropores is greater than that expected if the amount of N is the only parameter taken into account. This observation goes in line with the proposal that the most active sites for the ORR are hosted within the micropores [8]. Although our results demonstrate that active sites can be also created on carbon supports without micropores it is obvious that the presence of micropores results in more active catalysts for the ORR.

As described above, a careful inspection of Fig. 8 reveals that i_M increases linearly with the content of nitrogen in the CNTs but it appears to increase more rapidly for the samples in which microporosity has been developed, N/CNT-72 and N/CNT-150.

In order to understand the higher mass activity recorded for the electrocatalysts in which micropores have been formed the ORR pathway has been further studied. In principle, it is well accepted that the ORR can proceed *via* a direct reduction of O_2 to H_2O , the so-called 4 electrons pathway, or through the indirect reduction

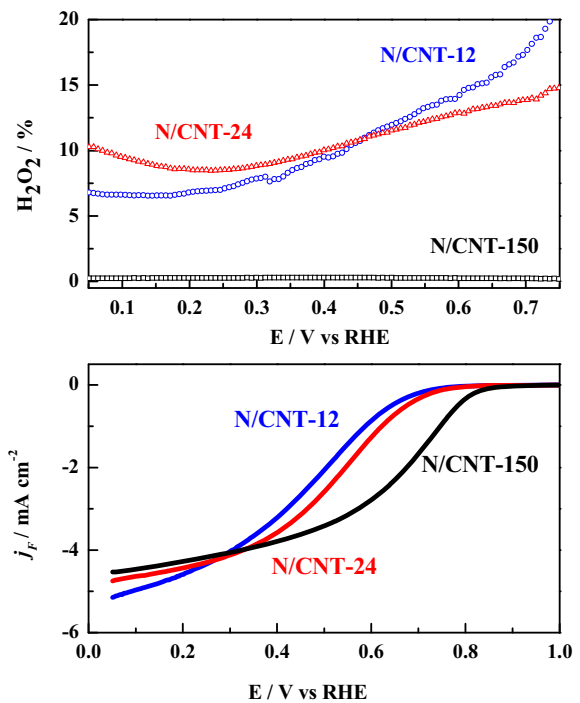


Fig. 9. Lower panel, positive going direction CV at 10 mV s^{-1} in O_2 saturated 0.1 M HClO_4 with N/CNT-t 12 (blue), 24 (red) and 150 (black) h. (0.6 mg cm^{-2}). Upper panel, simultaneously recorded H_2O_2 production (as determined for the ring currents) at 1600 rpm for a ring potential $E_R = 1.2 \text{ V}$. (For interpretation of the references to color in this figure legend, the reader is referred to the web version of this article.)

pathway, *i.e.*, through the formation of H_2O_2 . The production of H_2O_2 has been determined by recording RRDE experiments with catalysts in which micropores have been developed (N/CNT-150) and with two catalysts in which the CNT structure is intact but with different amounts of N (N/CNT-12 and N/CNT-24). Fig. 9 shows the production of H_2O_2 (%) recorded for N/CNT-12, N/CNT-24 and N/CNT-150.

As observed in Fig. 9, the production of H_2O_2 is different for the sample with micropores within their structure and for the samples without micropores. For the former, N/CNT-150, the production of H_2O_2 is low of *ca.* 1% increasing slightly at less positive potentials. On the contrary, both N/CNT-12 and N/CNT-24 record higher production of H_2O_2 , especially at potential values close to 0.75 V. More importantly, the production of H_2O_2 decreases as the potential is sweeped to less positive values. It appears like the direct reduction of O_2 , the so called $4e^-$ pathway, is favored in the catalysts with micropores whereas the $2e^-$ pathway, *i.e.*, O_2 reduction to H_2O_2 , is more important in the catalysts without micropores. It has been reported previously that the ORR on pyridinic-N and graphitic-N proceed *via* the 4- and 2-electrons pathways, respectively [18]. As shown in Table 2, the proportion of pyridinic-N and graphitic-N is similar in all of the catalysts reported in this work irrespective of their morphology. Therefore, the higher formation of H_2O_2 recorded with the catalysts in which the CNT structure is preserved cannot be justified by the presence of different chemical species or active sites. A possible explanation to justify the lower formation of H_2O_2 in the catalysts in which the active sites are located within micropores could be due to diffusional effects whereby H_2O_2 , which is formed within micropores, readsorbs and reacts easily onto the active sites responsible for the formation of H_2O before leaving the micropores. As a consequence, the amount of H_2O_2 actually detected in the RRDE experiments would be lower than that recorded with catalysts in which the readsorption process is not favored. On the other

hand, the readsorption of H₂O₂ and its further reduction to H₂O is not favored in catalysts with more open morphologies such as those based upon CNTs where once formed, H₂O₂ would reach the solution without further reaction.

4. Conclusions

By subjecting CNTs to ballmilling generates defects in the sp² carbon network are created. The number of such defects increases with ballmilling time. However, if the treatment is extended to 72 h or longer periods, the structure of the CNTs collapses and microporous carbon is formed. The incorporation of N into the graphite structure of the carbon obtained increases only moderately with the amount of defects but it increases significantly with the appearance of micropores. The N/CNT catalysts are active for the ORR in acid medium. In fact, the ORR performance of the N/CNT increases with the increasing amount of N in the final catalyst and as a consequence, the catalysts with the greater amount of N, which are those with the higher micropore area, are the most active in the series for the ORR.

Acknowledgements

This project was funded by the Deanship of Scientific Research (DSR), King Abdulaziz University, Jeddah, under grant number (D-006-432). The authors, therefore, acknowledge with thanks DSR technical and financial support. Economic support from Project 201080E116 from the CSIC is also acknowledged.

Appendix A. Supplementary data

Supplementary data associated with this article can be found, in the online version, at <http://dx.doi.org/10.1016/j.apcatb.2014.07.002>.

References

- [1] H.A. Gasteiger, S.S. Kocha, B. Sompalli, F.T. Wagner, *Appl. Catal., B: Environ.* 56 (2005) 9–35.
- [2] J.S. Spendelow, D.C. Papageorgopoulos, *Fuel Cells* 11 (2011) 775–786.
- [3] F. Jaouen, E. Proietti, M. Lefèvre, R. Chenitz, J.-P. Dodelet, G. Wu, H.T. Chung, C.M. Johnston, P. Zelenay, *Energy Environ. Sci.* 4 (2011) 114–130.
- [4] R. Jasinski, *Nature* 201 (1964) 1212–1213.
- [5] E. Proietti, F. Jaouen, M. Lefèvre, N. Larouche, J. Tian, J. Herranz, J.-P. Dodelet, *Nat. Commun.* 2 (2011) 416.
- [6] M. Lefèvre, E. Proietti, F. Jaouen, J.-P. Dodelet, *Science* 324 (2009) 71–74.
- [7] U.I. Kramm, J. Herranz, N. Larouche, T.M. Arruda, M. Lefèvre, F. Jaouen, P. Bogdanoff, S. Fiechter, I. Abs-Wurmbach, S. Mukerjee, J.P. Dodelet, *Phys. Chem. Chem. Phys.* 14 (2012) 11673–11688.
- [8] F. Jaouen, M. Lefèvre, J.-P. Dodelet, M. Cai, *J. Phys. Chem. B* 110 (2006) 5553–5558.
- [9] R. Franke, D. Ohms, K. Wiesener, *J. Electroanal. Chem.* 260 (1989) 63–73.
- [10] K. Wiesener, *Electrochim. Acta* 31 (1986) 1073–1078.
- [11] F. Jaouen, J. Herranz, M. Lefèvre, J.P. Dodelet, U.I. Kramm, I. Herrmann, P. Bogdanoff, J. Maruyama, T. Nagaoaka, A. Garsuch, J.R. Dahn, T. Olson, S. Pylypenko, P. Atanassov, E.A. Ustinov, *ACS Appl. Mater. Interfaces* 1 (2009) 1623–1639.
- [12] G. Wu, K.L. More, C.M. Johnston, P. Zelenay, *Science* 332 (2011) 443–447.
- [13] C. Domínguez, F.J. Pérez-Alonso, M. Abdel Salam, J.L. Gómez de la Fuente, S.A. Al-Thabaiti, S.N. Basahel, M.A. Peña, J.L.G. Fierro, S. Rojas, *Int. J. Hydrogen Energy*, 39 (2014) 5309–5318.
- [14] P.H. Matter, U.S. Ozkan, *Catal. Lett.* 109 (2006) 115–123.
- [15] P.H. Matter, E. Wang, M. Arias, E.J. Biddinger, U.S. Ozkan, *J. Phys. Chem. B* 110 (2006) 18374–18384.
- [16] V. Nallathambi, J.W. Lee, S.P. Kumaraguru, G. Wu, B.N. Popov, *J. Power Sources* 183 (2008) 34–42.
- [17] G. Wu, K.L. More, P. Xu, H.L. Wang, M. Ferrandon, A.J. Kropf, D.J. Myers, S. Ma, C.M. Johnston, P. Zelenay, *Chem. Commun.* 49 (2013) 3291–3293.
- [18] S. Yasuda, L. Yu, J. Kim, K. Murakoshi, *Chem. Commun.* 49 (2013) 9627–9629 (London, 1996).
- [19] L.G. Bulusheva, A.V. Okotrub, I.A. Kinloch, I.P. Asanov, A.G. Kurenya, A.G. Kudashov, X. Chen, H. Song, *Phys. Status Solidi B: Basic Res.* 245 (2008) 1971–1974.
- [20] H.R. Byon, J. Suntivich, E.J. Crumlin, Y. Shao-Horn, *Phys. Chem. Chem. Phys.* 13 (2011) 21437–21445.
- [21] J. Yang, D.J. Liu, N.N. Kariuki, L.X. Chen, *Chem. Commun.* (2008) 329–331.
- [22] U.I. Kramm, J. Herranz, N. Larouche, T.M. Arruda, M. Lefèvre, F. Jaouen, P. Bogdanoff, S. Fiechter, I. Abs-Wurmbach, S. Mukerjee, J.-P. Dodelet, *Phys. Chem. Chem. Phys.* 14 (2012) 11673–11688.
- [23] U.I. Kramm, M. Lefèvre, N. Larouche, D. Schmeisser, J.-P. Dodelet, *J. Am. Chem. Soc.* 136 (2013) 978–985.
- [24] F.J. Pérez Alonso, M.A. Salam, T. Herranz, J.L. Gómez de la Fuente, S.A. Al Thabaiti, S.N. Basahel, M.A. Peña, J.L.G. Fierro, S. Rojas, *J. Power Sources* 240 (2013) 494–502.
- [25] J.L.G. de la Fuente, S. Rojas, M.V. Martínez-Huerta, P. Terreros, M.A. Peña, J.L.G. Fierro, *Carbon* 44 (2006) 1919–1929.
- [26] U.A. Paulus, T.J. Schmidt, H.A. Gasteiger, R.J. Behm, *J. Electroanal. Chem.* 495 (2001) 134–145.
- [27] E. Proietti, S.p. Ruggeri, J.-P. Dodelet, *J. Electrochem. Soc.* 155 (2008) B340.
- [28] E. Proietti, J.-P. Dodelet, *ECS Trans.* 16 (2008) 393–404.
- [29] F. Jaouen, S. Marcotte, J.-P. Dodelet, G. Lindbergh, *J. Phys. Chem. B* 107 (2003) 1376–1386.
- [30] T. Herranz, S. Rojas, M. Ojeda, F.J. Pérez-Alonso, P. Terreros, K. Pirotta, J.L.G. Fierro, *Chem. Mater.* 18 (2006) 2364–2375.
- [31] G. Compagnini, *Carbon* 35 (1997) 1793–1797.
- [32] M. Dresselhaus, A. Jorio, M. Hofmann, G. Dresselhaus, R. Saito, *Nano Lett.* 10 (2010) 751–758.
- [33] P. Delhaes, M. Couzi, M. Trinquecoste, J. Dentzer, H. Hamidou, C. Vix-Guterl, *Carbon* 44 (2006) 3005–3013.
- [34] Y. Li, W. Zhou, H. Wang, L. Xie, Y. Liang, F. Wei, J.-C. Idrobo, S.J. Pennycook, H. Dai, *Nat. Nano* 7 (2012) 394–400.
- [35] M.S. Thorum, J.M. Hankett, A.A. Gewirth, *J. Phys. Chem. Lett.* 2 (2011) 295–298.
- [36] D. Strmcnik, M. Escudero-Escribano, K. Kodama, R. Stamenkovic/Vojislav, A. Cuesta, N.M. Marković, *Nat. Chem.* 2 (2010) 880–885.